

BIOPHYSICS

Leakless end-to-end transport of small molecules through micron-length DNA nanochannels

Yi Li¹, Christopher Maffeo², Himanshu Joshi^{2†}, Aleksei Aksimentiev^{2,3}, Brice Ménard⁴, Rebecca Schulman^{1,5*}

Designed and engineered protein and DNA nanopores can be used to sense and characterize single molecules and control transmembrane transport of molecular species. However, designed biomolecular pores are less than 100 nm in length and are used primarily for transport across lipid membranes. Nanochannels that span longer distances could be used as conduits for molecules between nonadjacent compartments or cells. Here, we design micrometer-long, 7-nm-diameter DNA nanochannels that small molecules can traverse according to the laws of continuum diffusion. Binding DNA origami caps to channel ends eliminates transport and demonstrates that molecules diffuse from one channel end to the other rather than permeating through channel walls. These micrometer-length nanochannels can also grow, form interconnects, and interface with living cells. This work thus shows how to construct multifunctional, dynamic agents that control molecular transport, opening ways of studying intercellular signaling and modulating molecular transport between synthetic and living cells.

INTRODUCTION

Nanoscale channels are fundamental mechanisms for directing transport across membranes in living systems. Synthetic nanopores and nanochannels that mimic the selectivity (1–3) and gating (4, 5) functions of biological membrane channels have become powerful tools in biosensing (6–8) and drug delivery (9, 10). Biomimetic channels assembled from different materials, such as peptides (11, 12), polymers (13), DNA (14), metal-organic complexes (15, 16), and carbon nanotubes (17), can mediate cross-membrane transport of a range of ions and molecules. Most of these biomimetic channels have diameters of less than 2 nm and thus allow transport of ions, but not larger molecular species.

Self-assembled DNA-based synthetic nanopores, particularly those built from scaffolded DNA origami, benefit from the extensive design space of DNA as building materials. DNA nanopores with inner diameters of more than 3 nm have been shown to mediate the passage of large biomolecules, such as double-stranded DNA and proteins, across lipid bilayer membranes (18–22). Moreover, highly predictable DNA interactions are the basis for the creation of programmable DNA nanopores that initiate transport only in the presence of specific chemical or spatial cues (20, 23). Advancements in DNA modifications using chemical groups and aptamers and control over pore geometries have further enabled selective transport of solute species across DNA nanopores (21, 24). In addition to their potential applications in biosensing and drug delivery (25), DNA nanopores can have functions as transporters in systems of synthetic cells (22): The lack of specificity of many types of membrane pores and the lack of reliable transport mechanisms

between synthetic cells are central challenges in reconstituting complex signaling systems in synthetic cells (26). The programmability and specificity of DNA nanopores could allow delivery of target genetic and signaling materials to make efficient communication possible.

However, existing large-diameter DNA nanopores have lengths of less than 100 nm and act as cross-membrane transporters (27, 28). Longer DNA-based channel structures, once built, could establish connections between nonadjacent cells or compartments for communication and molecular exchange. These channels could enable the development of complex transport networks that connect specific pairs of compartments in a synthetic tissue to create transport networks.

Here, we demonstrate bulk transport of molecules through micrometer-long DNA-based nanochannels and investigate the transport phenomena within them (Fig. 1A). DNA nanochannels that span up to several micrometers in length are self-assembled from double-crossover DNA tiles, on top of DNA origami pores with approximately 7-nm inner diameter. Observations that fluorescent dyes move across lipid membranes confirm that molecular transport can occur through both DNA pores and nanochannels. Further analysis of the kinetics of these processes suggests a continuum diffusion description of the transport within nanopores. By showing a DNA origami cap that closes the channel opening and prevents channel-mediated transport, we demonstrate specific gating of the nanochannel and that the transport is predominantly end to end rather than across channel walls.

The designed DNA nanochannels thus mediate leakless transport from one end of a channel to the other over distances ranging from tens of nanometers to micrometers, and this transport can be completely halted by the programmable binding of a DNA cap. The rates of transport in these channels are consistent with those in bulk solutions, allowing for precise design of flow rates. These advances suggest a toolkit of self-assembling elements for building nanoscale fluid transport networks to connect compartmentalized structures separated in space. These transport networks have great potential for studying intercellular communications and building artificial multicellular structures.

¹Department of Chemical and Biomolecular Engineering, Johns Hopkins University, Baltimore, MD 21218, USA. ²Department of Physics, University of Illinois Urbana-Champaign, Urbana, IL 61801, USA. ³Beckman Institute for Advanced Science and Technology, University of Illinois Urbana-Champaign, Urbana, IL 61801, USA.

⁴Department of Physics and Astronomy, Johns Hopkins University, Baltimore, MD 21218, USA. ⁵Department of Computer Science, Johns Hopkins University, Baltimore, MD 21218, USA.

*Corresponding author. Email: rschulm3@jhu.edu

†Present address: Department of Biotechnology, Indian Institute of Technology, Hyderabad-502 285, Telangana, India.

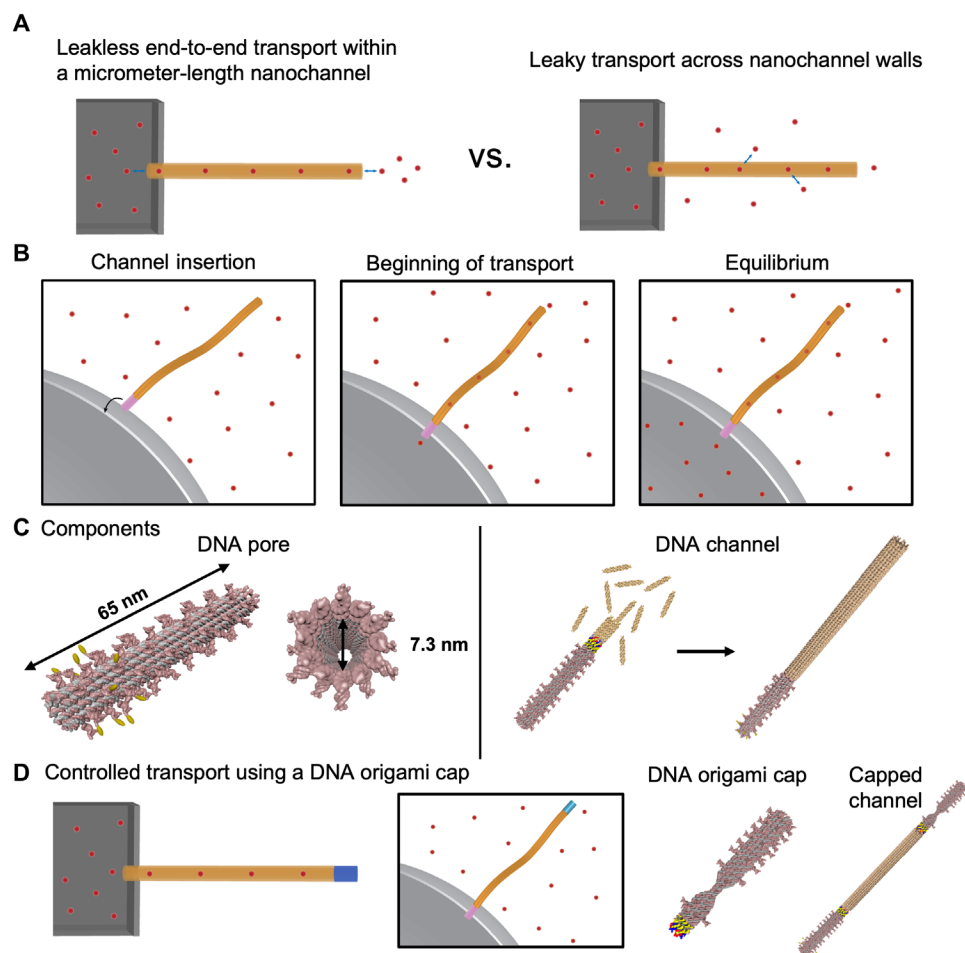


Fig. 1. Scheme for studying the transport of small molecules through micrometer-length self-assembled DNA nanochannels. (A) End-to-end transport of small molecules through micrometer-length channels could allow for controlled transport between channel end points. Diffusion across the channel walls leads to transport loss. (B) The assay used to characterize the rate of transport through a micrometer-long channel. When the channel attached to a pore enters a lipid membrane of a giant unilamellar vesicle (GUV), fluorescent dyes diffuse into the vesicle because of the concentration gradient across the membrane until equilibration of the concentration of fluorescent dyes inside and outside the vesicle. (C) A DNA origami nanostructure functionalized on one end with hydrophobic moieties serves as a transmembrane pore. DNA tiles hybridize to sticky ends on the DNA pore's opposite end to self-assemble a DNA nanotube hundreds of nanometers to micrometers in length that serves as a nanofluidic channel. (D) A cap that binds to and plugs the opening of the nanotube channel would prevent transport through the channel end into the vesicle but not transport across channel walls. A DNA channel cap with a designed constriction binds to the nanotube channel end via complementary DNA sticky ends.

RESULTS

Nanochannel design and structural characterization

To measure the rate of small-molecule transport through self-assembled DNA nanochannels, we first developed a DNA pore that could be inserted into lipid bilayer membranes. Molecules diffuse through the pore into a lipid vesicle, whose concentration is monitored over time (Fig. 1B). The DNA pore serves as both a submicrometer-length cross-membrane channel and as a template for the growth of micrometer-length nanochannels.

We constructed such a DNA pore by modifying a 12-helix scaffolded DNA origami cylinder of length 63.1 ± 1.8 nm, a nanotube seed (29) that can act as a template for DNA nanotube growth (Fig. 1C, left, and note S1). We added 15-nucleotide extensions to 12 of the staple strands near one end of the structure to which 12 cholesterol-conjugated single-stranded DNA strands could hybridize. The diameter of the pore was measured to be 7.3 ± 0.4 nm at the end of equilibrium coarse-grained molecular dynamics (MD)

simulations performed using the mrDNA package (fig. S4) (30). Electron micrographs of >100 pores (Fig. 2A and fig. S6) showed a mean length of 61.1 ± 0.5 nm, consistent with prior measurements via atomic force microscopy (29). Cholesterol-modified pores could spontaneously insert into the lipid bilayer membranes of small unilamellar vesicles (SUVs) at orientations generally perpendicular to the membranes (Fig. 2C).

We assembled longer nanochannels by growing nanotubes from the DNA pores hundreds of nanometers to several micrometers in length (notes S2 and S3) during an isothermal incubation at 37°C (Fig. 1C, right, and fig. S6). We then attached cholesterol-DNA conjugates to the pores. These channels could also interact with lipid bilayer membranes after being mixed with SUVs (Fig. 2D).

We designed a scaffolded DNA origami cap that binds to the open end of a DNA pore or a nanotube via sticky-end hybridization by modifying a rigid nanotube cap (Fig. 1D and fig. S3) (31). Pore-assisted small-molecule transport through capped channels

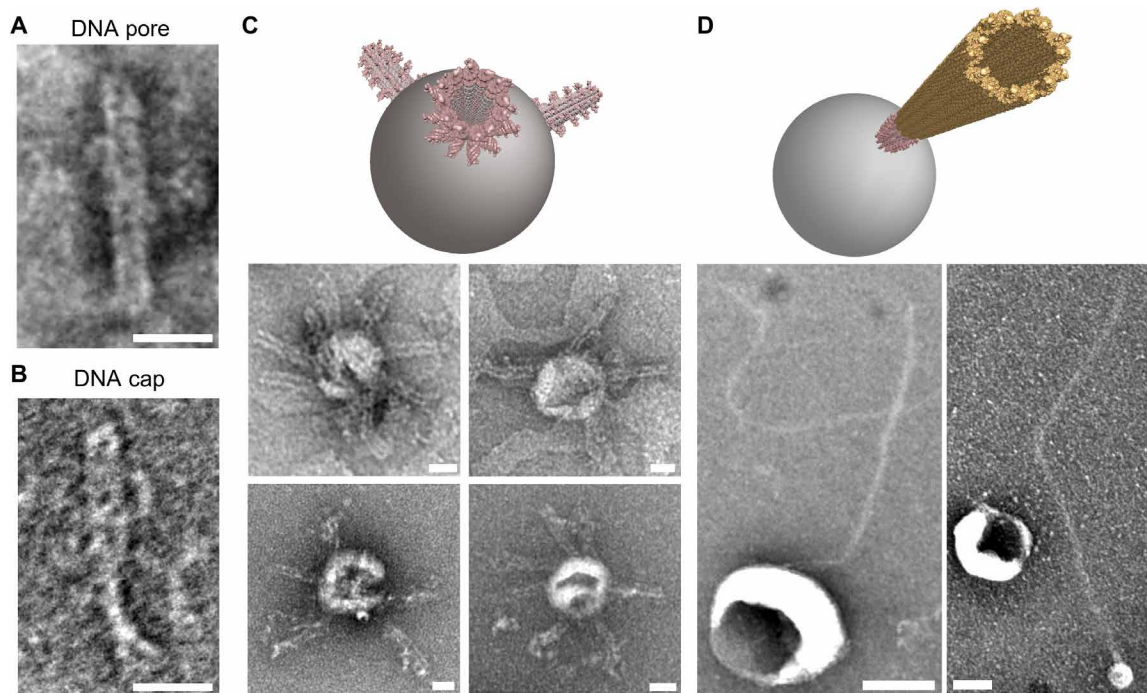


Fig. 2. Transmission electron microscopy (TEM) characterization of DNA pores and DNA nanotubes with SUVs. (A) Transmission electron micrograph of a DNA origami pore without DNA-cholesterol conjugates (note S4). (B) Transmission electron micrograph of a DNA channel cap. (C) Schematic and images of cholesterol-modified DNA origami pores interacting with SUVs. (D) Schematic and TEM images of cholesterol-modified DNA interacting with SUVs. Scale bars, 20 nm (A to C) and 100 nm (D).

could occur only if the small molecule could readily diffuse across channel walls, i.e., through interhelix gaps or structural defects. We thus hypothesized that, by comparing rates of pore-mediated molecular transport across capped and uncapped channels, we could determine whether nanochannels could direct the end-to-end transport of small molecules across their full lengths without loss through channel walls.

Transport rates through DNA pores suggest a continuum diffusion model

Controlling small-molecule transport through micrometer-long channels would be difficult if transport was mediated by specific molecule-surface interactions; molecule aggregation might also form clumps obstructing the channel. We therefore first sought to understand whether molecular transport occurs within the DNA channels by measuring rates of small-molecule transport through the pores (32, 33) and comparing these rates to the predictions of macroscopic diffusion models.

We tracked the flux of a fluorescent dye, carboxytetramethylrhodamine (TAMRA), through DNA pores into giant unilamellar vesicles (GUVs). TAMRA was selected for its small size, neutral charge, and low membrane permeability (34). GUVs were immersed in a TAMRA solution containing 1 nM DNA pores and were immobilized to a glass coverslip via biotin-streptavidin linkages. The rates of TAMRA influx into GUVs over a 3.2-hour duration were observed using time-lapse confocal microscopy.

The pores and membranes colocalized within the first 10 min. TAMRA then entered a much larger fraction of GUVs mixed with pores than GUVs without pores in control experiments (Fig. 3, A to C and G), demonstrating that the designed pores could facilitate transport across lipid membranes.

To quantify influx rates, we wrote computer programs to automatically identify 418 GUVs in micrographs and measured their internal fluorescence intensities over time. We computed the fractional fluorescence intensity (FFI) inside each vesicle, which we defined as the ratio of the mean fluorescence intensity inside a vesicle to the mean fluorescence intensity outside of vesicles in each field of view. The FFI of many vesicles initially increased slowly but then suddenly increased markedly. Initial rates of FFI increase were similar to rates the FFI increases in control experiments (Fig. 3C), suggesting that these initial increases were due to TAMRA slowly permeating through vesicle membranes. Although many pores adsorbed to membranes rapidly (Fig. 3B), this initial phase often lasted over 30 min, suggesting slow pore insertion kinetics, consistent with the high energy barrier to DNA origami pore insertion into GUVs observed previously (35).

Just one event of sudden increases in FFI was observed for most GUVs, indicating that either insertion of single pores or simultaneous insertion of multiple pores was most common. Multiple simultaneous insertions might occur if the insertion was a fusion event between a DNA pore-loaded SUV and a GUV. SUV by-products remained after GUV preparation, and the high membrane curvatures of small vesicles can promote DNA origami pore insertions (35). The pores were then transferred onto GUVs through vesicle fusions as vesicle fusions could frequently occur in solution, as has been observed previously (36, 37).

To better understand the rates of molecular transport, we developed a model that accounted for both fast, pore-mediated influx and slow influx due to TAMRA permeation across membranes. Fast TAMRA influx was modeled as net diffusion of TAMRA from the bulk solution outside the vesicle into a finite compartment through DNA pores (note S5). A DNA pore was modeled as a rigid cylindrical

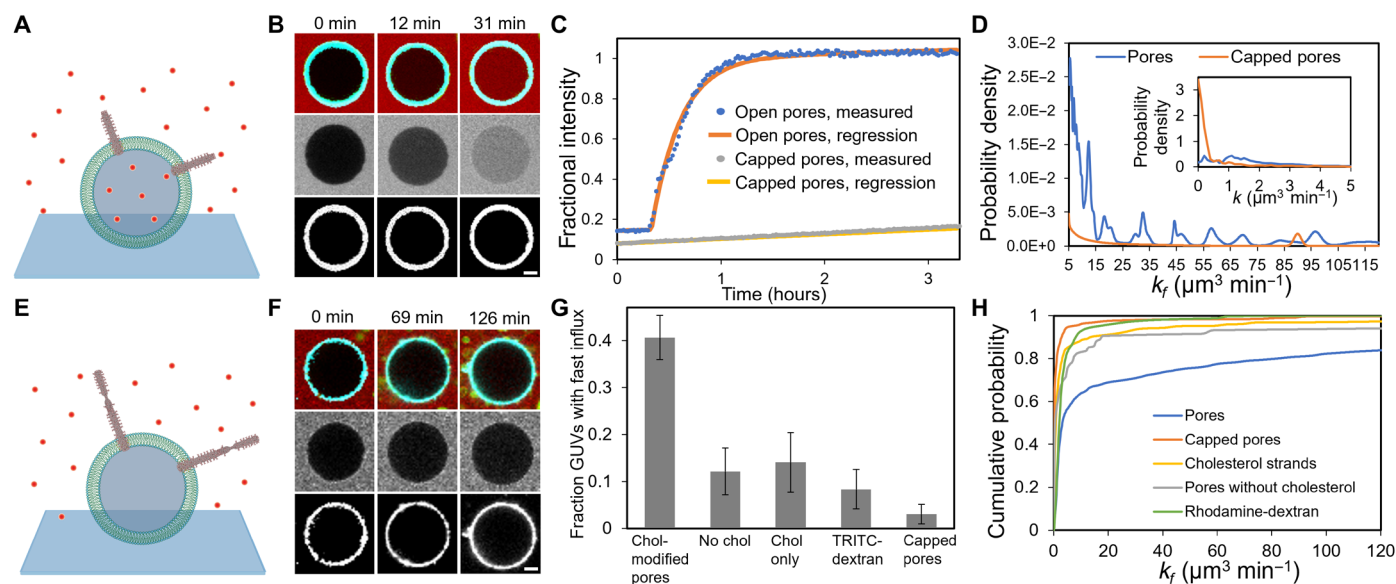


Fig. 3. TAMRA transport through open and capped DNA origami pores. (A) Dye (TAMRA) influx assay through DNA pores into GUVs. (B) Fluorescence micrographs of an example GUV during TAMRA influx as in (A). Top: Composite images of TAMRA (red), membrane (green), and DNA pores (cyan). Middle: TAMRA fluorescence. Bottom: DNA pore fluorescence. (C) Representative traces of fractional fluorescence intensities (FFIs) of GUVs during experiments as in (A) and (E). Pore-mediated influx begins after a lag period. Capped pores do not mediate influx. Regression curves of fractional intensities are best fits to Eq. 1 (note S10). (D) Distributions of GUV influx rates with DNA pores ($N = 418$) and capped DNA pores ($N = 264$). (E) Dye influx assay through capped DNA pores into GUVs. (F) Fluorescence micrographs of an example GUV. Little TAMRA enters the vesicle. Fluorescent labeling as in (B), except DNA caps (green) is also in the top-row micrographs. (G) Fractions of GUVs with fast influx ($k_f > 5 \mu\text{m}^3/\text{min}$) for (left to right) cholesterol-modified pores ($N = 418$), pores without cholesterol-DNA conjugates ($N = 165$), cholesterol-DNA conjugates ($N = 114$), pores and 500-kDa tetramethylrhodamine isothiocyanate-dextran (TRITC-dextran) dye in place of TAMRA ($N = 176$), and capped pores. Error bars are 95% confidence intervals. (H) Cumulative distributions of influx rates into GUVs from the pore, capped pore, and control experiments in (G).

channel with nonpermeable walls. Fick's law predicted that the flux of TAMRA at a given time should be linearly proportional to the difference in concentrations inside and outside the pore and to the total cross-sectional area of the inserted channels (33). Slow, non-pore-mediated TAMRA influx was modeled as a linear increase in fractional intensity (note S5)

$$f(t) = \begin{cases} f_0 + at & \text{when } t < t_1 \\ f_0 + at + (1 - f_0 - at_1) \left[1 - e^{-\frac{(t-t_1)}{\tau}} \right] & \text{when } t \geq t_1 \end{cases} \quad (1)$$

where $f(t)$ is FFI at time t . f_0 (initial FFI), a , τ , and t_1 (time when fast influx starts) are constant parameters.

Nonlinear regression produced good fits of the FFIs of most vesicles to Eq. 1; the small fraction of GUVs where the FFI increased in bursts, possibly due to lipid membrane defects (38), were excluded. We used these fits to calculate the fast (pore-mediated) influx rate ($k_f = \frac{V}{\tau}$), where V is the vesicle volume (note S9), and the background influx rate ($k_b = aV$) for each vesicle.

k_f represents the total influx rate due to multiple inserted pores on each vesicle. Because DNA origami pores each have the same lengths and diameters and thus the same expected rate of pore-mediated transport, influx rates from different numbers of inserted pores should be quantized rather than continuously distributed, with each quantum being the rate of influx through a single pore. Thus, analysis of the distribution of measured k_f can reveal the single-pore transport rate.

We summed the posterior distributions of k_f (to include measurement error) for the GUVs to produce a composite probability

distribution (Fig. 3D and note S10). The resulting distribution had a series of peaks. The Fourier transform of this distribution over 15 to 120 $\mu\text{m}^3/\text{min}$ had a dominant period of $13.1 \pm 1.5 \mu\text{m}^3/\text{min}$ (fig. S16). This measured value is very close to the first peak in the distribution ($12.4 \pm 2.5 \mu\text{m}^3/\text{min}$). Together, these results suggest that each pore mediated TAMRA influx at 12.4 to 13.1 $\mu\text{m}^3/\text{min}$, which corresponds to a net flux through each pore of 40.5 ± 4.6 molecules/s for the 309 nM TAMRA used in experiments (note S6).

The expected rate of TAMRA influx through a single pore following Fickian diffusion is $14.7 \pm 1.8 \mu\text{m}^3/\text{min}$ (note S11), almost precisely the measured rate of 12.4 to 13.1 $\mu\text{m}^3/\text{min}$. Although electrostatic interactions, van der Waals forces, and entry effects can play important roles in molecular transport in the nanoscale (39), the consistency between the measured TAMRA transport rates and the rates predicted by the continuum diffusion model suggested that the diffusion of TAMRA, a small uncharged molecule, in a DNA pore resembles molecular diffusion in a fluid continuum.

In the absence of pores, regression fits with Eq. 1 were almost uniformly below k_f of $5 \mu\text{m}^3/\text{min}$. In experiments with cholesterol-modified pores, a fraction of 0.41 ± 0.05 GUVs had $k_f > 5 \mu\text{m}^3/\text{min}$ (Fig. 3G), suggesting that cholesterol modification was necessary to induce fast influx. When TAMRA was replaced with the same concentration of a 500-kDa dye, tetramethylrhodamine isothiocyanate-dextran (TRITC-dextran) that has a hydrodynamic radius of 15.9 nm (40), a much lower percentage of GUVs (15%), had influx, demonstrating the size selectivity of the DNA pores. The nonzero percentage of vesicles that had influx in the control groups could suggest that a fraction of vesicles had impaired membranes, which possibly developed during vesicle preparation.

Because small gaps exist between DNA helices in DNA origami structures (41), pores could mediate transport by allowing TAMRA to diffuse from one end of the pore to the other or by allowing TAMRA to diffuse through gaps in the pore channels' helical walls. To determine whether TAMRA diffuses across channel walls, we measured the amount of flux mediated by pores bound to DNA origami caps (added in two times excess). Fluorescence micrographs revealed that a fraction of 0.97 ± 0.01 of pores was bound to caps (fig. S11). Capped pores localized to vesicle membranes, but fast TAMRA influx ($>5 \mu\text{m}^3/\text{min}$) occurred in only a fraction of 0.03 ± 0.02 of GUVs (Fig. 3, D to H). TAMRA therefore moves through pores via end-to-end diffusion and not through pore walls.

Molecules transport end to end through longer DNA nanochannels

To investigate whether TAMRA could also diffuse across a much longer nanochannel without leaking across its walls, we grew DNA tile nanotubes from pores as nanochannels. A total of $87 \pm 3\%$ of pores had nanochannels on them (fig. S6); their median length was $0.71 \mu\text{m}$ [95% confidence interval (CI) = $[0.64, 0.76] \mu\text{m}$] (Fig. 4C). There were sharp increases of FFI in many of the 167 tracked vesicles after initial lag periods (Fig. 4, A and B) in the dye influx experiment, implying that, like the DNA pores, DNA nanochannels mediated TAMRA flux across vesicle membranes.

Diffusive flux through channels should be inversely proportional to channel length (note S7), so the flux through nanochannels should be smaller than through pores. To test this hypothesis, we fit

the FFIs to Eq. 1. To collect as many measurements as possible, we included GUVs with two sequential insertion events in their FFI curves (note S10).

A fraction of 0.49 ± 0.08 vesicles had fast influx, i.e., $k_f > 1 \mu\text{m}^3/\text{min}$, much higher than the fraction in control experiments with nanotubes without cholesterol modification (Fig. 4G). The cumulative distribution of channel-mediated influx rates (Fig. 4H) was also shifted higher for nanochannels than for controls, confirming that most vesicle influx was induced by inserted nanochannels.

Because the lengths of the nanochannels are polydisperse, they should have different influx rates. Consistent with this, the cumulative distribution of flux rates was not quantized. To compare the measured influx rates with those predicted by a bulk diffusive model, we compared the medians of each distribution. The measured median k_f for GUVs with fast influx in the dye influx experiment was $3.3 \mu\text{m}^3/\text{min}$ (95% CI = $[1.9, 5.7] \mu\text{m}^3/\text{min}$). This measured rate was somewhat larger than the theoretical medium-length channel influx rate of $1.3 \mu\text{m}^3/\text{min}$, possibly because this comparison does not account for the presence of multiple channels on a single vesicle.

The lower rate of TAMRA flux through nanochannels than through pores suggested that the TAMRA was diffusing primarily across channel lengths, rather than across channel walls. To determine the extent to which TAMRA diffused from one end of a channel to the other, we measured the extent to which capped channels could mediate TAMRA influx. A fraction of 0.90 ± 0.04 nanochannels were bound to caps after incubating the nanochannels with caps (fig. S17). Fewer than 20% of vesicles had levels of TAMRA influx

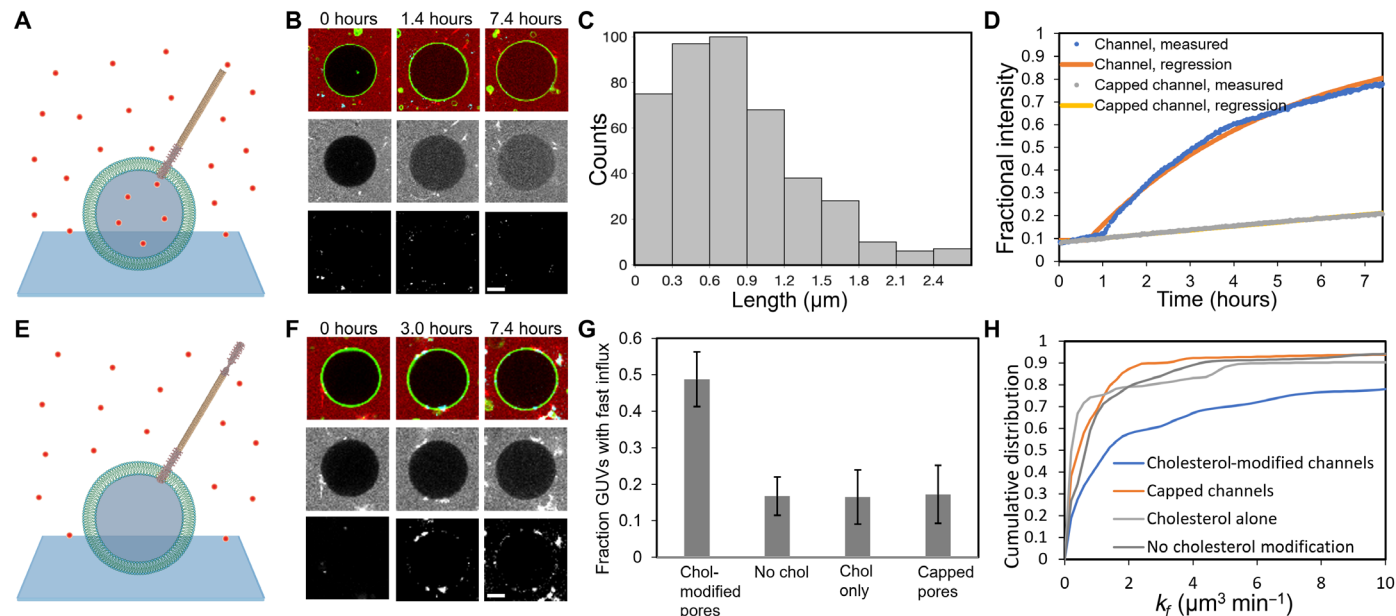


Fig. 4. Rates of dye diffusion through DNA nanotube channels suggest end-to-end diffusion through nanochannels. (A) TAMRA dye influx assay through DNA nanochannels. (B) Fluorescence micrographs of an example GUV at different time points during TAMRA influx into the vesicle. Fluorescence labeling is as described in Fig. 3B, except nanochannels (red) are in the same fluorescence channel as TAMRA. The vesicle size increases, potentially from small osmotic pressure imbalances, were accounted for when calculating influx rates. (C) Histogram of nanochannel lengths. The last bin accounts for lengths of $>2.4 \mu\text{m}$. (D) Representative FFI traces of a GUV in the experiment in (A) and a GUV from the experiment in (E). Regression curves are best fits to a Fickian diffusion model (note S10). (E) TAMRA dye influx assay through capped nanochannels. (F) Fluorescence micrographs of an example GUV in the capped nanochannel experiment with the same fluorescence labeling as in (B) except DNA caps (green). (G) Fractions of GUVs with fast TAMRA influx for the experiments in (A) and (E) and in control experiments where channels lack cholesterol modifications and with only cholesterol-DNA conjugates present. (H) The cumulative probability distribution of k_f between 0 and $10 \mu\text{m}^3/\text{min}$ measured in the experiments in (G) is calculated from the density distribution of k_f (fig. S15). Scale bars, $2 \mu\text{m}$ (B and F).

consistent with channel-mediated transport ($k_f > 1 \mu\text{m}^3/\text{min}$) in influx experiments with capped channels, indistinguishable from the percentage in control experiments (Fig. 4G). The cumulative distributions of k_f were also very close (Fig. 4H). DNA channel caps thus essentially eliminated most TAMRA flux through nanochannels, implying that the dominant mode of TAMRA flux was from one channel end to the other with a minimum loss across channel walls.

Evaluation of DNA-solute interactions through simulations

We used a combination of coarse-grained MD (30) and Brownian dynamics simulations (42) to probe microscopic parameters that govern the diffusion of small molecules through the ends and the walls of the DNA origami pore. In our coarse-grained simulations, each bead represented at least four DNA base pairs. To mimic partial incorporation of the nanostructures in a lipid bilayer membrane, the second to last turns of all DNA helices were subject to an external attractive potential (note S12). Over the course of a multi-resolution coarse-grained simulation, the DNA pore was observed to retain, on average, its cylindrical shape and undergo local structural fluctuations, transiently opening slit-like passages through the walls of the pore located between DNA helices away from the inter-helical crossovers (movie S4).

To evaluate conditions that facilitated diffusive end-to-end transport of small molecules, we transformed a representative equilibrated conformation of DNA pore into a three-dimensional (3D) potential describing the interaction of a point-like particle (e.g., a dye molecule) with the DNA structure and a 3D diffusivity map prescribing the local diffusion constant of the particle (note S12). The continuum model of the DNA nanopore was combined with a planar potential representation of a lipid membrane to produce a model of the DNA pore embedded in a lipid bilayer (Fig. 5A).

The model was surrounded by 396 point particles (corresponding to 4 mM concentration), and their diffusion in, around, and through the pore was simulated using the Brownian dynamics method (43). Note that, because of the point particle approximation, the dye molecules do not retain their asymmetric molecular shape in such a simulation. This approximation corresponds to a physical situation where reorientation of the molecule is faster than its passage through the nanostructure.

By varying parameters describing the DNA-particle interaction (Fig. 5B), we determined effective interactions that could account for experimental observations. Within the framework of our model, the physical size of the particle is prescribed by the effective contact distance σ , the closest proximity allowed between the center line of a DNA molecule and the center of the permeating solute. In a typical simulation, we counted the number of times a dye molecule entered the inner pore volume through the walls and the number of times a dye molecule entered through the top end of the pore. Figure 5 (C and D) shows how the number of both types of permeation events changes over the course of the simulations. A linear regression fit to the plots yielded the permeation rate. For a purely repulsive potential, the permeation of dye molecules through the walls dominates over the end-to-end transport at the effective contact distance σ of 16 Å or less (Fig. 5E). For $\sigma > 20$ Å, the rate of dye permeation through the end exceeds that through the walls. For $\sigma = 24$ and 28 Å, no through-the-wall permeation was observed, whereas molecules could still enter the nanopore through the end. Adding attraction to DNA-dye interaction makes both permeation events more likely (Fig. 5F) and shifts the crossover from wall- to end-dominated transport to higher values of effective contact distance. Together, our modeling results indicate that end-to-end transport through the pore becomes dominant when, at contact, the

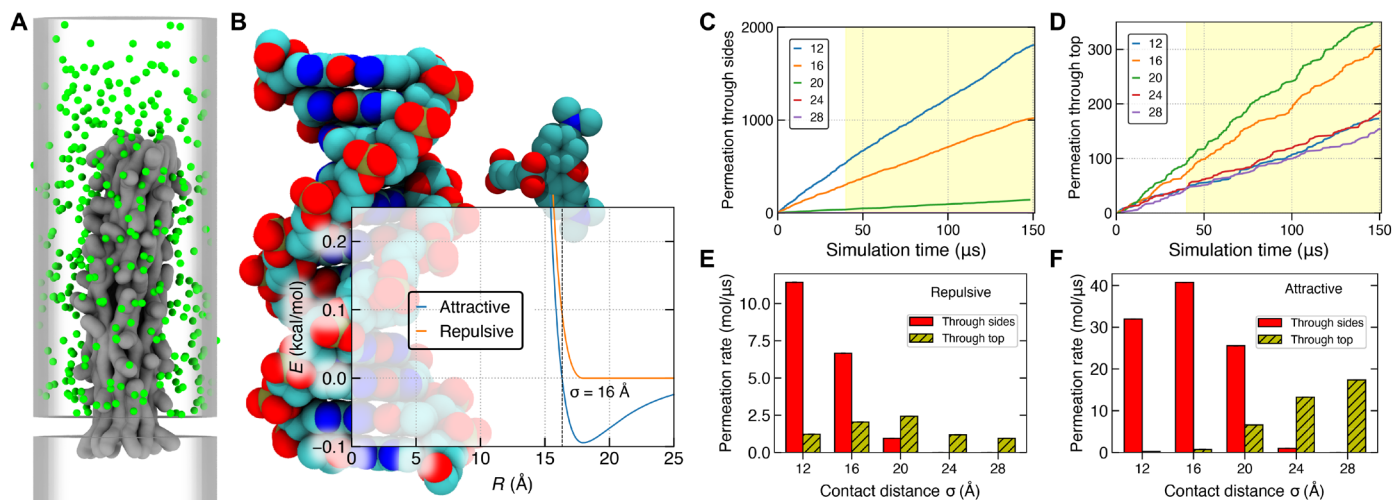


Fig. 5. Brownian dynamics simulation of a small-molecule permeation through the nanopore. (A) Representative configuration from a BD simulation of dye (green) diffusion through the nanopore structure. In the BD simulation of dye permeation, the bead-based representation of the nanostructure is replaced by grid-based interaction potential (gray; 1 kcal mol^{-1} isosurface) and a local diffusivity map. (B) Examples of the attractive and repulsive interaction potential between DNA and a dye molecule. All-atom models of a DNA duplex and of a TAMRA dye are shown approximately to scale in the background. Parameter σ defines effective contact distance. (C and D) The number of dye molecules permeated through the side walls (C) and through the top entrance (D) of the nanopore as a function of simulation time for purely repulsive models of dye-nanostructure interaction. The models vary by the value of the contact distance parameter σ (in angstroms). No side wall permeation was observed for σ of 24 or 28 Å. (E) The average rate of dye permeation computed using a linear regression fit to the data shown in (C) and (D) (shaded regions). The rate is much higher than in the experiment because of a much higher dye concentration used in the BD simulations. (F) The average rate of dye permeation for several models of attractive dye-DNA interaction.

distance between the center of the solute and the center of the DNA helix exceeds 2 nm, which corresponds, approximately, to solutes greater than 0.8 nm in radius.

DISCUSSION

Here, we have designed DNA origami pores and micrometer-long DNA nanochannels that could spontaneously insert into GUV membranes. Dye influx assays enabled measurements of the kinetics of small-molecule diffusion into the GUVs. These kinetic measurements verified that both DNA pore and DNA nanochannels could transport small molecules at rates predicted by the continuum diffusion model. Last, binding of a DNA cap to either a DNA pore or DNA nanochannel's end stopped transport, demonstrating that transport is end to end with minimal leak across the channel. This end-to-end transport through a nanochannel can direct how a molecule diffuses well beyond the spanning ends of a membrane; it could presumably enable transport between two compartments that are micrometers apart.

The self-assembled nanochannels studied here can self-repair (44) and form interconnects between molecular landmarks (45), suggesting how they might be used to form nanoscale flow networks for building artificial multicellular systems, widely used in studying cell-to-cell signaling. Large channel diameters could allow the transport of macromolecules such as proteins and DNA. Long channel lengths would also be advantageous for characterizing the DNA-protein or protein-protein interactions within a channel because the residence time should scale with the square of channel length, allowing more time for characterization in a longer channel than in a short one. Functionalizing nanotube interiors with antibodies or DNA aptamers could also allow nanotube channels to be used for detecting proteins of interest or other biosensing applications.

MATERIALS AND METHODS

Materials

All DNA oligodeoxynucleotides were purchased from Integrated DNA Technologies (Coralville, IA, USA), except the 7240–base pair M13mp18 scaffold strand purchased from Bayou Biolabs (Los Angeles, CA, USA). Tris/acetate/EDTA (TAE) buffer was purchased from Thermo Fisher Scientific (Waltham, MA, USA). Ninety-six–well glass-bottom plates with a streptavidin coating were purchased from Arrayit (Sunnyvale, CA, USA; catalog no. M96S). TAMRA was purchased from Sigma-Aldrich (St. Louis, MO, USA). All lipids were purchased from Avanti Polar Lipids (Alabaster, AL, USA). TRITC-dextran of average molecular weight of 4400 Da was purchased from MilliporeSigma (St. Louis, MO, USA; catalog no. T1037).

DNA pore assembly

A mixture containing 5 nM scaffold strand, 200 nM staple strand mix, and 25 nM attachment strand mix (note S1) was first prepared in TAE Mg^{2+} buffer (40 mM tris-acetate and 1 mM EDTA) with 12.5 mM magnesium acetate added (TAEM) (note S4.1). The assembly mixture was subjected to a thermal annealing ramp with an Eppendorf Mastercycler (note S3.3). The assembled pores were then purified to remove excessive DNA strands using a 100-kDa molecular weight cut-off (MWCO) Amicon Ultra centrifugal filter device (MilliporeSigma). Following purification, 0.15 μ l of 100 μ M ATTO647-modified DNA

strand that hybridizes to binding sites on attachment strands was added to 40- μ l purified pore sample and incubated at room temperature for 15 min to allow to fluorescently label the pores. The concentration of fluorescently labeled pores was approximately 1 nM, determined by measuring the concentration of a stock solution by counting the number of pores per field of view (86 μ m by 86 μ m) adsorbed to a glass slide from a specific reaction volume in fluorescence micrographs captured using a fluorescence microscope (Olympus, IX71) with a 60 \times /1.45 numerical aperture (NA) oil immersion objective lens and a \times 1.6 magnifier lens. To modify the DNA pores with cholesterol, 1 μ l of DNA-cholesterol conjugate (note S3.6) at 10 μ M was incubated at 50°C for 10 min to alleviate cholesterol aggregation before being added to 40 μ l of purified DNA pores. The solution was then incubated for 10 min at room temperature.

DNA nanotube channel assembly

DNA nanotube channels were self-assembled from DNA tiles and DNA pores. DNA tile monomers in an inactive form and DNA pores with adapters that presented monomer sticky ends were separately prepared before being mixed to form nanotube channels. Inactive DNA monomers were prepared by mixing six strands that fold into inactive monomers (note S2), each at 400 nM in TAEM, and by subjecting the mixture to a thermal annealing ramp (note S3.4). To make DNA pores with adapters, the nanopore assembly mixture was prepared as in the “DNA pore assembly” section except that 100 nM adapter strands were added to the mixture before thermal annealing (note S3.2). After assembly, the pores were purified and concentrated to 2 nM and then fluorescently labeled (note S3.4). Twenty microliters of pores were then mixed with 20 μ l of inactive monomers and 0.2 μ l of monomer activation strand (50 μ M). The sample was then incubated at 37°C for at least 15 hours to allow the nanotubes to grow. DNA-cholesterol conjugates were then hybridized to the pore regions of the nanotube channels by following the same steps used for modifying pores before influx assays.

SUV preparation

Five milligrams of 1,2-diphytanoyl-*sn*-glycero-3-phosphocholine (DPhPC; Avanti Polar Lipids, USA) was dissolved in 1 ml of chloroform in a glass vial. The solvent was evaporated by blowing nitrogen gas into the glass vial for 20 min so that a dry lipid film was formed. The glass vial was kept in a vacuum desiccator overnight to remove any residual solvent. One milliliter of 150 mM potassium chloride solution was then added to the glass vial to hydrate the lipid film. SUVs were then formed by 2-hour sonication in a bath sonicator [Bransonic Ultrasonic Cleaner (1510R-DTH)] at 40°C. The SUVs were diluted 1000 times with 150 mM potassium chloride before use.

Transmission electron microscopy

A formvar/carbon film support grid (Electron Microscopy Sciences, Hatfield, PA, USA; catalog no. FCF400-Cu) was glow-discharged in a vacuum for 40 s. Ten microliters of sample to be imaged was prepared (note S4). The grid was put onto the sample droplet and was incubated at room temperature for 5 to 10 min. The sample solution was then washed off by tapping the grid on MilliQ water droplets five times. The sample attached to the grid was stained by immediately tapping the grid on 2% (w/w) uranyl acetate (Electron Microscopy Sciences, Hatfield, PA, USA; catalog no. 22400) solution droplets twice, followed by a 5-min incubation on the uranyl

acetate solution. The solution was then blotted, and the grid was first dried using a filter paper and then dried in air for at least an hour. The grid was imaged using a field emission FEI Technai-12 electron microscope operated at 100-keV voltage.

GUV preparation

The protocol for preparing GUV was adapted from Horger *et al.* (46) with modifications. One percent (w/w) agarose in deionized water was boiled in a microwave oven. Two hundred microliters of the warm agarose solution was poured onto a glass-bottom dish. The dish was kept on a hot plate at 80°C for an hour to form a dry agarose film. DPhPC lipids and 1,2-dioleoyl-*sn*-glycero-3-phosphoethanolamine-*N*-(biotinyl) (biotinyl PE) were dissolved in chloroform to a concentration of 5 mg/ml in glass vials. A fluorescent lipid, 1-palmitoyl-2-(dipyrrometheneboron difluoride)undecanoyl-*sn*-glycero-3-phosphocholine (TopFluor PC), was dissolved in chloroform to a concentration of 1 mg/ml in a glass vial. The three lipid solutions were mixed in chloroform to prepare a lipid mix solution (1 mg/ml) with a composition of 88% DPhPC, 10% biotinyl PE, and 2% TopFluor PC. Forty microliters of lipid mix solution was then deposited onto the dry agarose film on the dish. The dish was kept in a vacuum desiccator overnight to allow the lipid solution to completely dry. After solvent was removed, 300 μ l of 0.2 M sucrose solution was added to the film in the dish. The dish was kept undisturbed at room temperature for 2 days to allow GUV formation.

Dye influx assay setup

Ninety microliters of TAE buffer supplemented with 0.2 M sucrose and 309 nM TAMRA was added into a well on a 96-well glass-bottom plate with a streptavidin coating. Six microliters of GUV solution was then added into the well. The GUVs encapsulating 0.2 M sucrose settled down onto and became immobilized on the glass surface in about 5 min due to density differences between the solutions inside and outside the GUVs and biotin-streptavidin binding between the vesicles and the glass surface. Thirty-five microliters of solution containing either pores, capped pores, nanotube channels, or capped nanotube channels prepared in TAEM buffer, after cholesterol modification, was mixed with 9 μ l of 1 M glucose before being added into the well to maintain a final concentration of 0.2 M glucose. The final concentration of magnesium ions was 3.1 mM.

The sample on the glass-bottom plate was imaged on an inverted confocal microscope (Nikon Ti2-E with A1 confocal unit) using a 60 \times /1.49 NA oil immersion objective lens. DNA pores were imaged using a 640-nm diode laser, TAMRA and DNA nanotubes were imaged using a 560-nm diode laser, and GUVs were imaged using a 480-nm diode laser. All three fluorescent channels at one focal plane position in a large area of 4 \times 4 fields of view were captured with 60- or 71-s time intervals. Each field of view had dimensions of 512 \times 512 pixels, corresponding to a physical field-of-view size of 210 μ m by 210 μ m. The experiments with DNA pores were observed for a total time length of 210 min, and experiments with DNA nanotubes were observed for a total time length of 8 hours. The Nikon Perfect Focus System was used to eliminate axial focus fluctuations. The dye influx experiments with DNA pores were repeated twice, and experiments with nanotubes were repeated once to ensure that fluorescence measurements of over 100 GUVs were collected.

Fluorescence image data processing

To quantify the fluorescence intensities of TAMRA over time inside and outside GUVs observed using confocal microscopy, we first

used ImageJ software to identify and track individual GUVs captured. The outlines of GUVs at each time point were identified by applying the “thresholding” function in ImageJ software to convert the grayscale images of GUVs into binary images. The image areas inside GUVs at each time point were identified by selecting the areas separated by GUV outlines that had circularities greater than 0.65 using the “Analyze Particles” function in ImageJ software. Similarly, one area outside GUVs at each time point was identified by selecting the largest area in the image with circularity smaller than 0.6. The mean fluorescence intensities of TAMRA in the areas inside and outside the identified GUVs at each time point were measured from grayscale images of TAMRA. The TAMRA concentration fractions of individual GUVs at each time point were calculated by dividing the mean intensities inside GUVs to the mean intensity outside GUVs.

SUPPLEMENTARY MATERIALS

Supplementary material for this article is available at <https://science.org/doi/10.1126/sciadv.abq4834>

[View/request a protocol for this paper from Bio-protocol.](#)

REFERENCES AND NOTES

1. S. W. Kowalczyk, T. R. Blosser, C. Dekker, Biomimetic nanopores: Learning from and about nature. *Trends Biotechnol.* **29**, 607–614 (2011).
2. F. De Riccardis, I. Izzo, D. Montesarchio, P. Tecilla, Ion transport through lipid bilayers by synthetic ionophores: Modulation of activity and selectivity. *Acc. Chem. Res.* **46**, 2781–2790 (2013).
3. X. Hou, W. Guo, F. Xia, F. Q. Nie, H. Dong, Y. Tian, L. Wen, L. Wang, L. Cao, Y. Yang, J. Xue, Y. Song, Y. Wang, D. Liu, L. Jiang, A biomimetic potassium responsive nanochannel: G-Quadruplex DNA conformational switching in a synthetic nanopore. *J. Am. Chem. Soc.* **131**, 7800–7805 (2009).
4. V. Maingi, M. Lelimosin, S. Howorka, M. S. P. Sansom, Gating-like motions and wall porosity in a DNA nanopore scaffold revealed by molecular simulations. *ACS Nano* **9**, 11209–11217 (2015).
5. K. Zhao, H. Wu, Structure-dependent water transport across nanopores of carbon nanotubes: Toward selective gating upon temperature regulation. *Phys. Chem. Chem. Phys.* **17**, 10343–10347 (2015).
6. L. Liu, H.-C. Wu, DNA-based nanopore sensing. *Angew. Chem. Int. Ed.* **55**, 15216–15222 (2016).
7. H. Bayley, P. S. Cremer, Stochastic sensors inspired by biology. *Nature* **413**, 226–230 (2001).
8. W. Shi, A. K. Friedman, L. A. Baker, Nanopore sensing. *Anal. Chem.* **89**, 157–188 (2017).
9. A. Koçer, M. Walko, W. Meijberg, B. L. Feringa, A light-actuated nanovalve derived from a channel protein. *Science* **309**, 755–758 (2005).
10. R. Duan, F. Xia, L. Jiang, Constructing tunable nanopores and their application in drug delivery. *ACS Nano* **7**, 8344–8349 (2013).
11. G. W. Gokel, S. Negin, Synthetic ion channels: From pores to biological applications. *Acc. Chem. Res.* **46**, 2824–2833 (2013).
12. J. Montenegro, M. R. Ghadiri, J. R. Granja, Ion channel models based on self-assembling cyclic peptide nanotubes. *Acc. Chem. Res.* **46**, 2955–2965 (2013).
13. J. G. Neevel, R. J. M. Nolte, Ion transport across vesicle bilayers mediated by an artificial channel compound. *Tetrahedron Lett.* **25**, 2263–2266 (1984).
14. M. Langecker, V. Arnaut, T. G. Martin, J. List, S. Renner, M. Mayer, H. Dietz, F. C. Simmel, Synthetic lipid membrane channels formed by designed DNA nanostructures. *Science* **338**, 932–936 (2012).
15. R. Kawano, N. Horike, Y. Hijikata, M. Kondo, A. Carné-Sánchez, P. Larpent, S. Ikemura, T. Osaki, K. Kamiya, S. Kitagawa, S. Takeuchi, S. Furukawa, Metal-organic cuboctahedra for synthetic ion channels with multiple conductance states. *Chem* **2**, 393–403 (2017).
16. T. M. Fyles, C. C. Tong, Long-lived and highly conducting ion channels formed by lipophilic ethylenediamine palladium(II) complexes. *New J. Chem.* **31**, 655–661 (2007).
17. B. Liu, X. Li, B. Li, B. Xu, Y. Zhao, Carbon nanotube based artificial water channel protein: Membrane perturbation and water transportation. *Nano Lett.* **9**, 1386–1394 (2009).
18. S. Krishnan, D. Ziegler, V. Arnaut, T. G. Martin, K. Kapsner, K. Henneberg, A. R. Bausch, H. Dietz, F. C. Simmel, Molecular transport through large-diameter DNA nanopores. *Nat. Commun.* **7**, 12787 (2016).
19. K. Göppfrich, C. Y. Li, M. Ricci, S. P. Bhamidimarri, J. Yoo, B. Gyenes, A. Ohmann, M. Winterhalter, A. Aksimentiev, U. F. Keyser, Large-conductance transmembrane porin made from DNA origami. *ACS Nano* **10**, 8207–8214 (2016).

20. R. P. Thomsen, M. G. Malle, A. H. Okholm, S. Krishnan, S. S.-R. Bohr, R. S. Sørensen, O. Ries, S. Vogel, F. C. Simmel, N. S. Hatzakis, J. Kjems, A large size-selective DNA nanopore with sensing applications. *Nat. Commun.* **10**, 5655 (2019).
21. T. Diederichs, G. Pugh, A. Dorey, Y. Xing, J. R. Burns, Q. H. Nguyen, M. Tornow, R. Tampé, S. Howorka, Synthetic protein-conductive membrane nanopores built with DNA. *Nat. Commun.* **10**, 5018 (2019).
22. S. Iwabuchi, I. Kawamata, S. Murata, S.-i. M. Nomura, A large, square-shaped, DNA origami nanopore with sealing function on a giant vesicle membrane. *Chem. Commun.* **57**, 2990–2993 (2021).
23. Q. Yang, Z. Guo, H. Liu, R. Peng, L. Xu, C. Bi, Y. He, Q. Liu, W. Tan, A cascade signaling network between artificial cells switching activity of synthetic transmembrane channels. *J. Am. Chem. Soc.* **143**, 232–240 (2021).
24. A. Barati Farimani, P. Dibaeinia, N. R. Aluru, DNA origami–graphene hybrid nanopore for DNA detection. *ACS Appl. Mater. Interfaces* **9**, 92–100 (2017).
25. B. Shen, P. Piskunen, S. Nummelin, Q. Liu, M. A. Kostianen, V. Linko, Advanced DNA nanopore technologies. *ACS Appl. Bio Mater.* **3**, 5606–5619 (2020).
26. B. Sharma, H. Moghimianavval, S.-W. Hwang, A. P. Liu, Synthetic cell as a platform for understanding membrane-membrane interactions. *Membranes* **11**, 912 (2021).
27. S. Howorka, Building membrane nanopores. *Nat. Nanotechnol.* **12**, 619–630 (2017).
28. Z. Zhao, H. Yan, Y. Liu, A route to scale up DNA origami using DNA tiles as folding staples. *Angew. Chem.* **122**, 1456–1459 (2010).
29. A. M. Mohammed, R. Schulman, Directing self-assembly of DNA nanotubes using programmable seeds. *Nano Lett.* **13**, 4006–4013 (2013).
30. C. Maffeo, A. Aksimentiev, MrDNA: A multi-resolution model for predicting the structure and dynamics of DNA systems. *Nucleic Acids Res.* **48**, 5135–5146 (2020).
31. D. K. Agrawal, R. Jiang, S. Reinhardt, A. M. Mohammed, T. D. Jorgenson, R. Schulman, Terminating DNA tile assembly with nanostructured caps. *ACS Nano* **11**, 9770–9779 (2017).
32. H. Mehrer, Continuum theory of diffusion, in *Diffusion in Solids* (Springer Series in Solid-State Sciences, 2007), vol. 155, pp. 27–28.
33. G. L. Flynn, S. H. Yalkowsky, T. J. Roseman, Mass transport phenomena and models: Theoretical concepts. *J. Pharm. Sci.* **63**, 479–510 (1974).
34. L. Wang, M. Tran, E. D'Este, J. Roberti, B. Koch, L. Xue, K. Johnsson, A general strategy to develop cell permeable and fluorogenic probes for multicolour nanoscopy. *Nat. Chem.* **12**, 165–172 (2020).
35. J. R. Burns, S. Howorka, Defined bilayer interactions of DNA nanopores revealed with a nuclease-based nanoprobe strategy. *ACS Nano* **12**, 3263–3271 (2018).
36. C. K. Haluska, K. A. Riske, V. Marchi-Artzner, J.-M. Lehn, R. Lipowsky, R. Dimova, Time scales of membrane fusion revealed by direct imaging of vesicle fusion with high temporal resolution. *Proc. Natl. Acad. Sci. U.S.A.* **103**, 15841–15846 (2006).
37. L. Chen, S. Liang, Y. Chen, M. Wu, Y. Zhang, Destructing the plasma membrane with activatable vesicular DNA nanopores. *ACS Appl. Mater.* **12**, 96–105 (2020).
38. E. Karatekin, O. Sandre, H. Guitouni, N. Borghi, P.-H. Puech, F. Brochard-Wyart, Cascades of transient pores in giant vesicles: Line tension and transport. *Biophys. J.* **84**, 1734–1749 (2003).
39. W. Sparreboom, A. van den Berg, J. C. T. Eijkel, Principles and applications of nanofluidic transport. *Nat. Nanotechnol.* **4**, 713–720 (2009).
40. J. K. Armstrong, R. B. Wenby, H. J. Meiselman, T. C. Fisher, The hydrodynamic radii of macromolecules and their effect on red blood cell aggregation. *Biophys. J.* **87**, 4259–4270 (2004).
41. S. Fischer, C. Hartl, K. Frank, J. O. Rädler, T. Liedl, B. Nickel, Shape and interhelical spacing of DNA origami nanostructures studied by small-angle x-ray scattering. *Nano Lett.* **16**, 4282–4287 (2016).
42. J. Comer, A. Aksimentiev, Predicting the DNA sequence dependence of nanopore ion current using atomic-resolution Brownian dynamics. *J. Phys. Chem.* **116**, 3376–3393 (2012).
43. D. L. Ermak, J. A. McCammon, Brownian dynamics with hydrodynamic interactions. *J. Chem. Phys.* **69**, 1352–1360 (1978).
44. Y. Li, R. Schulman, DNA nanostructures that self-heal in serum. *Nano Lett.* **19**, 3751–3760 (2019).
45. A. M. Mohammed, P. Šulc, J. Zenk, R. Schulman, Self-assembling DNA nanotubes to connect molecular landmarks. *Nat. Nanotechnol.* **12**, 312–316 (2017).
46. K. S. Horgor, D. J. Estes, R. Capone, M. Mayer, Films of agarose enable rapid formation of giant liposomes in solutions of physiologic ionic strength. *J. Am. Chem. Soc.* **131**, 1810–1819 (2009).
47. S. Jia, S. C. Phua, Y. Nihongaki, Y. Li, M. Pacella, Y. Li, A. M. Mohammed, S. Sun, T. Inoue, R. Schulman, Growth and site-specific organization of micron-scale biomolecular devices on living mammalian cells. *Nat. Commun.* **12**, 5729 (2021).
48. D. Y. Zhang, R. F. Hariadi, H. M. T. Choi, E. Winfree, Integrating DNA strand-displacement circuitry with DNA tile self-assembly. *Nat. Commun.* **4**, 1965 (2013).
49. S. M. Douglas, A. H. Marblestone, S. Teerapittayanon, A. Vazquez, G. M. Church, W. M. Shih, Rapid prototyping of 3D DNA-origami shapes with caDNAno. *Nucleic Acids Res.* **37**, 5001–5006 (2009).
50. P. Šulc, F. Romano, T. E. Ouldridge, L. Rovigatti, J. P. Doye, A. A. Louis, Sequence-dependent thermodynamics of a coarse-grained DNA model. *J. Chem. Phys.* **137**, 13510 (2012).
51. G. Octobre, C. Lemerrier, S. Khochbin, M. Robert-Nicoud, C. Souchier, Monitoring the interaction between DNA and a transcription factor (MEF2A) using fluorescence correlation spectroscopy. *C. R. Biol.* **328**, 1033–1040 (2005).
52. N. S. Cheng, Formula for the viscosity of a glycerol-water mixture. *Ind. Eng. Chem. Res.* **47**, 3285–3288 (2008).
53. J. F. Comesaña, J. J. Otero, E. García, A. Correa, Densities and viscosities of ternary systems of water + glucose + sodium chloride at several temperatures. *J. Chem. Eng. Data* **48**, 362–366 (2003).

Acknowledgments: We sincerely thank S. Jia, N. Niranjani, and S. Schaffter for useful discussions. **Funding:** Y.L. and R.S. acknowledge support from the Defense Advanced Research Projects Agency (D16AP00147) and the Department of Energy (DE-SC0010426). C.M., H.J., and A.A. acknowledge support from the National Science Foundation of USA (DMR-1827346) and the supercomputer time provided through the XSEDE allocation grant (MCA055028) and Leadership Resource Allocation MCB20012 on Frontera of the Texas Advanced Computing Center. **Author contributions:** Y.L. and R.S. planned and designed the experiments. Y.L. conducted the experiments. Y.L. and B.M. performed data analysis. C.M., H.J., and A.A. performed simulations. Y.L., R.S., C.M., H.J., and A.A. wrote the paper. All authors discussed the results and commented on the manuscript. **Competing interests:** The authors declare that they have no competing interests. **Data and materials availability:** All data needed to evaluate the conclusions in the paper are present in the paper and/or the Supplementary Materials. Computer codes used in this study are publicly available at DOI: 10.5281/zenodo.6644202.

Submitted 12 April 2022

Accepted 21 July 2022

Published 7 September 2022

10.1126/sciadv.abq4834